This manuscript is the post-print version of the paper "Computational MHD analyses in support of the design of the WCLL TBM breeding zone" published in Fusion Engineering and Design, volume 170, September 2021, 112535, doi: https://doi.org/10.1016/j.fusengdes.2021.112535. Hereby we declare that is consistent with the published paper.

# Computational MHD analyses in support of the design of the WCLL TBM breeding zone

Alessandro Tassone*, Gianfranco Caruso

*DIAEE Nuclear Section - Sapienza University of Rome, Corso Vittorio Emanuele II, 244, 00186, Roma, Italy*

**Abstract**

The Water-Cooled Lithium Lead (WCLL) is a blanket concept pursued in the framework of Test Blanket Module (TBM) campaign in ITER. Even if the liquid metal is circulated slowly in the component, magnetohydrodynamic (MHD) pressure losses are still expected to be significant.

The aim of this paper is to assess the MHD pressure losses in the TBM frontal part, also called Breeding Zone (BZ). There, important contributions are caused by the manifold interface, the presence of cooling pipes obstructing the fluid movement, a sharp hairpin bend, and non-uniform wall thickness of the walls. Direct numerical simulation of 2D and 3D MHD flows is used to estimate the head loss for each one of these elements.

A scaling law is derived to allow quick estimate of the pressure loss from reference parameters. The main contribution to the head loss is caused by the windows that connect the BZ with the manifold.

*Keywords:* Magnetohydrodynamics (MHD), pressure drop, WCLL blanket, Liquid metals, ITER, TBM

## 1. Introduction

A moving electrically conductive fluid in presence of an imposed magnetic field is subjected to self-induced Lorenz forces that oppose the fluid motion and, thus, greatly increase the pressure drop [1]. The estimate of these so-called magnetohydrodynamic (MHD) losses is of great interest for liquid metal blanket engineering. This study aims to consider this problem for the case of the Breeding Zone (BZ) of the Water-Cooled Lithium Lead (WCLL) Test Blanket Module (TBM) [2, 3]. A similar work has been performed by the Kalrsruhe Institute of Technology focusing on the manifold [4].

The dimensionless MHD momentum equation is formulated for an incompressible, induction-less, and laminar flow as

$$\frac{1}{\mathrm{N}}\left[\frac{\partial u}{\partial t}+(u\cdot\nabla)u\right]=-\nabla p+\frac{1}{\mathrm{Ha}^2}\nabla^2 u+J\times B \qquad (1)$$

in which $\mathrm{N}=\sigma B_0^2 a/\rho u_0$ is the interaction parameter, characteristic ratio of electromagnetic/inertial forces, and $\mathrm{Ha}=B_0 a(\sigma/\mu)^{1/2}$ is the Hartmann number, representative of the electromagnetic/viscous force balance [1]. An additional dimensionless group is introduced to describe the relationship between the electric resistance offered to the fluid currents by the fluid boundary layer and the bounding wall. This quantity, called wall conductance ratio, is expressed with $\mathrm{c_w}=\sigma_w t_w/\sigma a$, where $t_w$ is the wall thickness. For fusion applications, N and Ha assume typically large ($\approx 10^4$) but finite values, whereas $c_w = 10^{-2} - 10^{-1}$. In the WCLL TBM, Equation (1) must be solved in its complete form to estimate the MHD pressure drop. Neglecting friction losses, $\Delta p = \Delta p_{2D} + \Delta p_{3D}$ in which the right-hand terms stand for the analogues of hydraulic distributed and concentrated losses [5]. The former are characteristic of fully developed flows, where currents are constrained to the duct cross-section, while the latter are caused by stream-wise $\partial_x u$ (*viz.* electric potential, $\partial_x \phi$), which are responsible for additional currents. The pressure scale is $p_0 = \sigma u_0 B_0^2 a$ where $u_0 = 0.25$ mm s$^{-1}$ is the BZ mean velocity , $B_0 = 3.9$ T is the toroidal field intensity [6, 7], and $a = 96.75$ mm is the BZ channel toroidal half-width [8]. Conductivity ($\sigma$), density ($\rho$), and viscosity ($\mu$) are considered constant and evaluated at $T_0 = 600$ K for fluid (PbLi, from [9]) and solid (Eurofer from [10]) materials.

The focus of this numerical study is on developing scaling laws for the MHD pressure loss occurring in the WCLL TBM. These are useful to guide the component design and for implementation in systems codes like RELAP5 [11, 12], MHD-SYS [13], and others [14, 15]. Full flow characterization has been performed for all the analyses considered in this study but, in order to keep the present paper to an acceptable length, will be the subject of a forthcoming work.

## 2. Problem geometry and definition

The WCLL TBM design is strongly based on the European DEMO WCLL "driver" BB in order to ensure rele-

*Corresponding author: alessandro.tassone@uniroma1.it

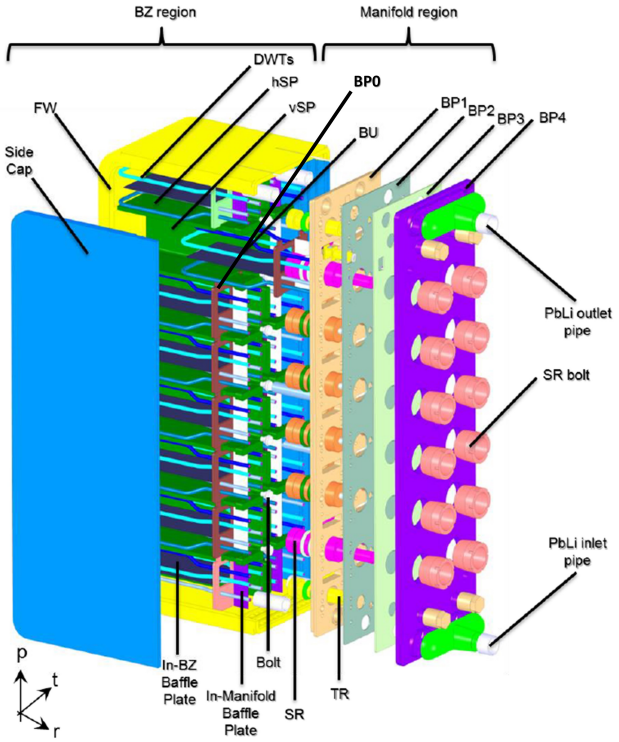


**Figure 1:** Exploded view of the WCLL TBM and sub-components of manifold and BZ: Double Walled Tubes (DWT), horizontal and vertical Stiffening Plates (hSP/vSP, in green), First Wall (FW), Breeding Unit (BU), Back Plate ($BP_i$). Reproduced with permission from Ref. [8].

vancy of the data that will be gathered during the ITER experimental campaigns [3, 8, 16]. An exploded view of the TBM is presented in Figure 1. The module is essentially divided in two areas: the BZ and the manifold. The former constitutes the frontal section, being delimited by the side caps, the U-shaped First Wall (FW), and the Back Plate (BP0). The BZ is further divided into 16 Breeding Units (BUs) by a system of horizontal and vertical Stiffening Plates (SPs). Double Walled Tube (DWT) U-pipes are inserted in the BUs and carry the refrigerant (pressurized water at 15.5 MPa), which is tasked with BZ power extraction. The manifold region is delimited by the side caps, FW, BP0 and BP4. The region that is allocated to the breeder flow path is contained between BP0 and BP1.

The internal stiffening structures and cooling pipe arrangement is shown in more detail in Figure 2. The BU constitutes the basic geometric element of the TBM BZ and, depending on its position, it can be distinguished into a top, bottom or central BU. In the following, our attention is going to be focused on the central BU that is the most typical element; top and bottom BU have a similar layout, but are slightly larger in the poloidal dimension. BUs are stacked in two poloidal assemblies composed by 8 elements each (1 top, 1 bottom, 6 central). The "left" and "right" assembly, with reference to Figure 2b, are characterized by a different cooling pipe layout. For the purpose of this study, we are going to consider only the central "right" BU.

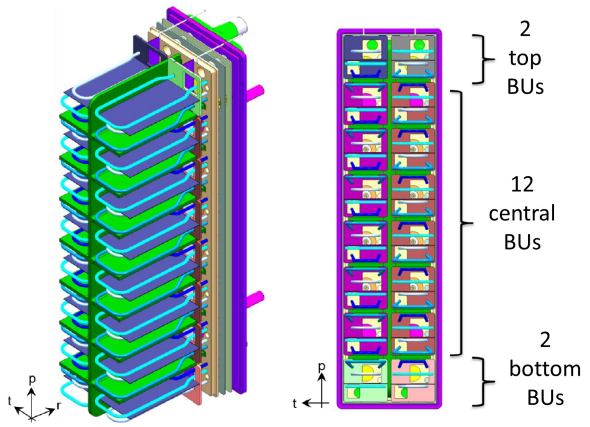


**(a)** Isometric view **(b)** Poloidal-toroidal view

**Figure 2:** WCLL TBM internal stiffening structures and DWTs grid. Reproduced with permission from Ref. [8].

Considerations from this basic geometry can readily be extended to the other BUs. Note that the cooling pipe layout is not radially invariant but, rather, the pipes undergo a geometric transition between the back and the front of the radial channel with the shift of the poloidal position and/or a toroidal pitch enlargement/shrinking.

The selected geometry is presented in Figure 3. The breeder flow path in the BU is divided by a thin baffle plate into an inlet (bottom) and an outlet (top) radial channel. These are joined together close to the FW. Each BU channel is thus delimited by a hSP, a side cap, the vSP, and the baffle plate, as it is shown in Figures 3a and 3b. Note that all these structures have a different thickness. Square windows drilled in BP0 allow the free passage of the liquid metal from the manifold to the BZ. The PbLi is flowing poloidally from the bottom to the top of the TBM in the manifold: the distribution and collection manifold legs are separated by a thin in-manifold baffle plate (see Figures 1 and 3c). Part of the distribution leg flow is diverted radially to feed a BU through the inlet window. Then, the liquid metal flows, again radially, within the BU, as shown in Figures 3a and 3c, reverses its direction close to the FW executing a sharp 180° turn, and, finally, is conveyed out through the outlet window, after flowing in the top channel. The flow exiting the BU curves poloidally and joins the main manifold flow in the collection leg.

The nominal operation state and operational domain of the PbLi in the WCLL TBM is still under evaluation [17]. Breeder conditions are going to be very close to what is expected in the WCLL BB for EU DEMO, in order to ensure relevancy of the experimental data and maximize return of experience [3, 16]. For the BU mean velocity, $u_0 = 0.25\ \mathrm{mm\,s^{-1}}$ is a realistic value with regard to the BB design, where it is optimized to reduce MHD losses and for tritium extraction purposes, which corresponds to a TBM mass flow rate of $0.59\ \mathrm{kg\,s^{-1}}$ [5, 16–18]. Toroidal magnetic field intensity can be calculated from the reference data for ITER since $B_t(R_0) = 5.3$ T and $B_t(R)R = const$, where

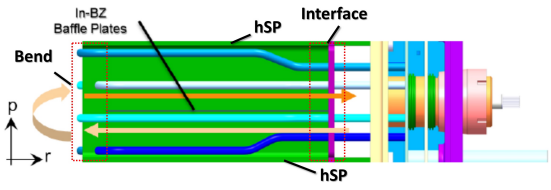


**(a)** Poloidal-radial view

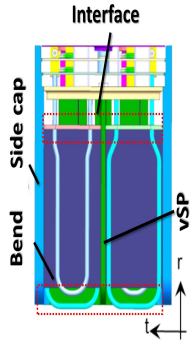


**(b)** Radial-toroidal

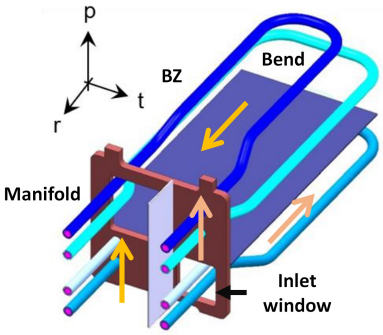


**(c)** Isometric view

**Figure 3:** WCLL TBM BZ: flow path, general layout and interface with manifold. Reproduced with permission from Ref. [8].

$R_0 = 6.2$ m is the tokamak major radius and $R$ is the radial coordinate [5, 6]. The TBM is going to be placed on the outboard section, therefore we can evaluate the $B_t$ average value in the BU from the approximate position of the BU centroid: $R^* = R_0 + a + L/2$, where $a = 2$ m is the tokamak minor radius and $L = 0.43$ m stands for the BU radial channel length. It follows from $B_t(R_0)R_0 = B_t(R^*)R^*$ that $B_t(R^*) = B_0 = B_t(R_0)R_0/R^* \approx 3.9$ T.

A complete 3D MHD simulation of the BZ flow has been deemed unfeasible given the computational resources available to the authors and the time-frame of the study. The hydraulic elements contributing to the pressure loss have been studied separately in order to derive a comprehensive scaling law to use for design purposes. Essentially, three situations can be identified: the BZ/manifold transition through the interface window, the fully developed radial flow in presence of cooling pipes aligned with the stream-wise direction, and a change of stream direction (hairpin bend) in the presence of transverse obstacles.

Connection to the manifold via windows entails significant cross-section variation in the magnetic field direction, which is expected to dominate interface pressure loss, and has been studied in Section 4. Fully developed flow is expected within the BZ and $\Delta p_{2D}$ is estimated in Section 5 accounting for the presence of walls with different thickness, obstacles, and coupling between the counter-flowing ducts. Finally, the loss due to the hairpin bend is discussed in Section 6.

## 3. Numerical strategy

Direct numerical simulation of Equation (1) is accomplished using the general purpose CFD code ANSYS CFX [19]. To estimate the Lorentz force source term in Equation (1), additional equations must be defined to calculate the electromagnetic variables. Due to the induction-less approximation, $B$ is a boundary condition of the problem and $J$ is the only variable to be determined [1]. This is accomplished by the solution of Ohm's law

$$J = -\nabla\phi + u \times B \tag{2}$$

where an additional variable, the electric potential $\phi$, is introduced that, in turn, is calculated through

$$\nabla^2\phi = \nabla \cdot (u \times B). \tag{3}$$

Equations (1) to (3) with the addition of the continuity equation $\nabla \cdot u = 0$ compose the governing equations for the MHD flow.

No-slip boundary condition (u=0) is imposed at the fluid/solid interface. Velocity inlet and zero pressure outlet are adopted for the 3D models discussed in Sections 4 and 6. In these cases, the fully developed MHD velocity profile for average velocity $\overline{u} = u_0$ is given at the inlet. Accurate velocity profiles are obtained from dedicated 2.5D simulations adopting translational periodicity to simulate an infinitely long duct[1] with a flowing mass flow rate $\Gamma = \rho u_0 A$, where $A$ is the duct cross-section. This same strategy is adopted for the 2.5D model used to study the fully developed flow in Section 5.

Since the TBM walls feature finite conductivity, electric currents can flow both in the fluid and surrounding walls. Electromagnetic variables are calculated with a conjugate method assuming conservation at the fluid/solid interface, i.e. $\phi = \phi_w$ and $J_n = J_{n,w}$. At the wall external surfaces, a Neumann boundary condition, $\partial\phi = 0$, is applied to satisfy charge conservation ($\nabla \cdot J = 0$), as well as at the inlet and outlet. It should be highlighted that, in general, currents can flow through neighboring BUs due to the electrically conductive walls and that coupling phenomena between adjacent BUs and across the TBM at large are expected to influence both the flow features and the pressure loss, see Section 7.1.2. To this extent, a Neumann boundary condition for the external walls cannot be considered entirely realistic but, nevertheless, is necessary to reduce the computational domain to a manageable size.

The magnetic field is assumed to be constant, uniform, and unidirectional with the only non-null component being the toroidal one. In general, a poloidal component is always present in the TBM, such that $B_p = B_t/3$ [7]. The inclined magnetic field affects the current distribution in

[1] Formally, a 2D model is the minimum requirement to solve this type of problems, but CFX lacks the support for reduced dimensionality of the governing equations [20]. A 2.5 model featuring between two and four nodes in the "empty" direction must be used instead.

**Table 1:** Physical properties of PbLi [9] and Eurofer steel [10] at $T_{\text{ref}} = 600$ K

| Property (unit) | Symbol | PbLi | Eurofer |
|---|---|---|---|
| Density (kg m$^{-3}$) | $\rho$ | $9.806 \times 10^3$ | |
| Electrical conductivity (S m$^{-1}$) | $\sigma$ | $8.747 \times 10^5$ | $1.145 \times 10^6$ |
| Dynamic viscosity (Pa s) | $\mu$ | $1.928 \times 10^{-3}$ | |
| Magnetic permeability (H m$^{-1}$) | | $\mu_0$ | $\mu_0$ |

the liquid metal and its effect on pressure loss is discussed in Section 7.1.1.

Volumetric heating in the BU is neglected and the flow is assumed to be isothermal. Uncertainty introduced on pressure loss estimate by neglecting magneto-convective phenomena are briefly discussed in Section 7.1.4. Physical properties of PbLi and Eurofer are constant and are listed in Table 1.

Diffusion and pressure gradient terms are evaluated using tri-linear shape functions. A fully implicit method, which solves the momentum and pressure-based continuity equation together, is used to ensure the pressure-velocity coupling. The second-order bounded upwind "High Resolution" scheme is adopted to discretize advection terms and calculation is performed with the CFX pseudo-transient steady-state algorithm [19]. Convergence is assumed to be reached when RMS residuals are below $10^{-4}$ and all the monitor points of the local solution are stationary.

Details about code validation can be found in [21, 22]. Mesh sensitivity is assessed for each numerical model using a minimum of three grids of increasing resolution. Characteristic pressure and velocity values are monitored to determine the result independence. A complete overview of the mesh sensitivity procedure is available in Ref. [23] for all the studied cases, whereas an example pertaining to the window model is discussed in Section 4.1.

## 4. Interface with manifold

The connection between BZ and manifold features significant geometrical complexity, as shown in Figures 1 and 3: the transition from a poloidal to a radial flow, important cross-section variation, and the presence of cooling pipes that partially obstruct the manifold channel and the BU windows. A comprehensive numerical analysis of the interface would require considering all these effects, in addition to inclined field and coupling, but it has been deemed unfeasible for the purpose of a first scoping study. The choice has been made to focus on the likely most relevant contribution to the pressure loss, leaving the assessment of a more realistic configuration to future studies.

It has been assumed that the BZ/manifold interface can be described as a first approximation with the sudden variation of cross-section along the magnetic field direction occurring when the flow passes through the BP0 orifices, i.e. the inlet and outlet window. The effect of cooling pipes, the poloidal-to-radial 90° turn, and the presence of

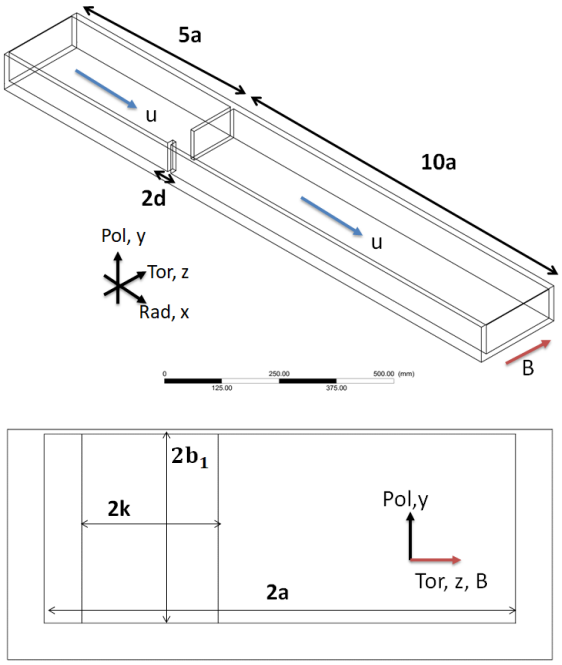


**Figure 4:** Inlet window numerical model. Top: Isometric view of the channel. Bottom: Detail of window and channel cross-section variation.

the dominant manifold flow have been neglected. Moreover, the flow is assumed to be fully developed and perfectly radial when entering our numerical model. The simplified numerical model geometry is shown in Figure 4, where the axis origin is placed at the geometrical center of the BP, and characteristic geometric parameters are presented in Table 2, alongside those that are relevant also for calculations presented in Sections 5 and 6.

The velocity gradient generated by the passage through the BP0 orifice causes the induction of current loops that are responsible for a $\Delta p_{3D}$. The cross-section variation is described by the characteristic ratio between the window ($k$) and main channel toroidal half-widths, $Z = a/k$, called change ratio. The analysis has been focused on the inlet window, which is characterized by the largest change ratio, i.e. $Z_I = 3.46$ against $Z_O = 2.3$ [24, 25]. The effect of the minor poloidal contraction ($Z_p \approx 1.3$) has been ignored since, being perpendicular to $B$, should not contribute noticeably to the pressure loss [26]. Simulations have been performed for $0 \leq \text{Ha} \leq 4 \times 10^3$ and $1 \leq \text{Re} = \text{Ha}^2 / \text{N} \leq 1.25 \times 10^4$.

### *4.1. Mesh sensitivity*

To demonstrate the independence of the numerical results from the grid resolution, a mesh sensitivity was carried over with the test case at Ha = 500 and Re = 130 as a template. Five grids of increasing resolution were generated, as shown in Table 3; mesh0 to mesh2 increased the grid axial resolution, mesh3 to mesh4 refined toroidally mesh1, and mesh5 enhanced the resolution of mesh4 in both directions.

**Table 2:** BU geometrical parameters. Lengths are reported in mm.

| | | |
|---|---|---|
| Toroidal half-width | $a$ | 96.75 |
| Window tor half-width | $k$ | 28 |
| Poloidal half-height (bottom channel) | $b_B$ | 38.75 |
| Poloidal half-height (top channel) | $b_T$ | 54 |
| Duct wall thickness | $t_w$ | 15 |
| Baffle plate thickness | $t_b$ | 2 |
| Back plate (BP) thickness | $2d$ | 10 |

**Table 3:** Mesh sensitivity on selected variables for the window model. $N$ represents the number of elements.

| Mesh | N $\times 10^6$ | $\Delta p$(Pa) | $\Delta p_{3D}$(Pa) | $u_{Max}$ (mm s$^{-1}$) |
|---|---|---|---|---|
| 0 | 6.714 | 1.70259 | 0.39417 | 6.211257 |
| 1 | 7.976 | 1.64101 | 0.37155 | 6.215702 |
| 2 | 9.357 | 1.71221 | 0.38949 | 6.220608 |
| 3 | 8.430 | 1.71494 | 0.38612 | 6.222636 |
| 4 | 9.100 | 1.71282 | 0.38781 | 6.221222 |
| 5 | 12.289 | 1.71227 | 0.38918 | 6.226487 |

A basic description of the MHD flow occurring in the BU identifies three main flow regions, cfr Figure 5. In the center of the channel, the flow is dampened and the velocity profile is flat. This region is called "core" and is characterized by negligible viscous and inertial effects, so that the main force balance is between the pressure gradient and Lorentz force [1]. More than one core region may be present for complex geometries, as it will be shown in Section 5.2. Walls that are parallel to the field, called "sidewalls", are characterized by the formation of high velocity jets in their boundary layers. This feature is characteristic of electrically conductive walls and depends on the value of $c_w$, as it is going to be discussed in Section 5.1. Finally, the last flow region is the Hartmann layers, which are formed at walls perpendicular to the field (not shown in Figure 5), which are characterized by steep velocity gradients. Adequate mesh resolution in Hartmann and sidewall layers is fundamental for computation of MHD flows. For the interface model, this requirement is aggravated by an adequate resolution in internal layers that are formed where the channel geometry undergoes a relevant change and propagate along field lines [27].

The mesh sensitivity results have been evaluated both qualitatively and quantitatively for velocity, electric potential, and pressure. Results are presented in Figure 5 and Table 3 for some selected variables. A minimum mesh resolution of 8 nodes for the Hartmann layer and between 20 and 30 for sidewall and internal layers is found to be necessary to achieve mesh independence. Mesh4 is chosen as the reference grid for the window model.

### *4.2. Results and discussion*

Fluid transfer between window and upstream (downstream) core is mostly occurring through internal layers

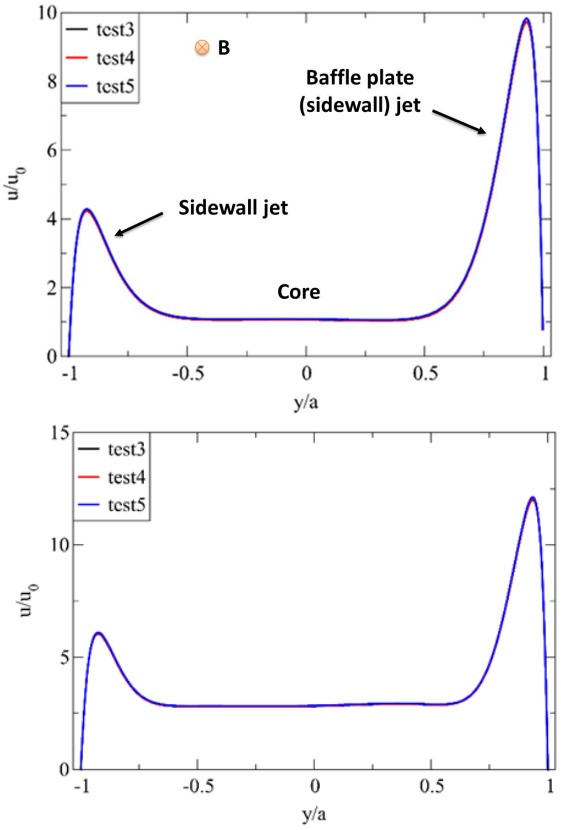


**Figure 5:** Velocity profile in window model between sidewalls downstream (top picture, x = -10 mm, z = 53 mm) and at the window center (bottom, x = 0 mm, z = 53 mm) for three selected grids.

that develop along field lines from the juncture between differently sized channels, as demonstrated in Figure 6. Velocity gradient between the main channel and the smaller orifice induces a potential difference that drives axial currents, as it is schematically shown in Figure 7a. These currents are associated to the 3D MHD flow observed at the interface and induce additional Lorentz forces that cause the so-called three-dimensional pressure loss. Fluid is pushed from the core toward the sidewalls, promoting the jets there, upstream and within the orifice, whereas the opposite happens downstream, as demonstrated in Figure 7b. This phenomenon is superimposed to the toroidal fluid transfer happening in the internal layer. An example is shown in Figure 8 of the transition in the current distribution from the purely 2D fully developed flow upstream of the orifice and the 3D pattern established downstream of it, where closed current loops are observed in the internal layers.

An electromagnetic-viscous-inertial force balance is established in the internal layers and affects both the entity of the three-dimensiona loss and the flow structure. Depending on the value assumed by the characteristic ratio $N/Ha^{3/2}$, the flow pattern shifts either toward inertia-dominated ($N/Ha^{3/2} \ll 1$) or inertia-less ($N/Ha^{3/2} \gg 1$) flow regimes [26, 28, 29]. The internal layer is observed to change its structure depending on the flow regime with the

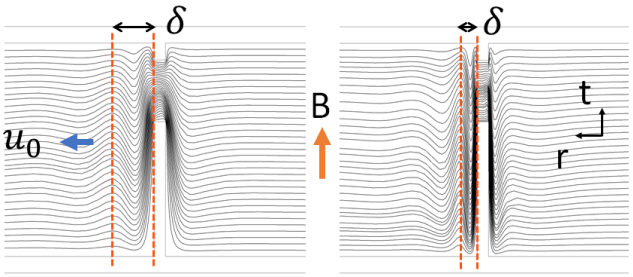


**Figure 6:** Velocity streamlines at window center. Left: Ha = 500, right: Ha = 4000. Interal layer marked only for downstream expansion.

dimensionless internal layer thickness $\delta \propto \mathrm{N}^{-1/3}$ for the inertia-dominated regime and $\delta \propto \mathrm{Ha}^{-1/2}$ for the inertia-less one [25, 29, 30].

Interface loss is calculated as in Figure 9a. It is assumed that $\Delta p_{3D} = \Delta p - \Delta p_{2D}$, where $\Delta p_{2D}$ is taken as the pressure loss for a fully developed flow in a duct without orifice. It is observed that $\Delta p_{3D}$ depends on the flow regime and it can be described with two expressions based on the dimensionless internal layer thickness. For the inertia-dominated regime, $\Delta p_{3D}$ for the inlet window can be approximated by

$$\Delta p_{\mathrm{W,I}} = 0.1984 + 1.5531\ \mathrm{N}^{-1/3} \tag{4}$$

where 10 data points in the range $2.416 \times 10^{-3} \leq \mathrm{N}\,/\,\mathrm{Ha}^{3/2} \leq 0.487$, $100 \leq \mathrm{Ha} \leq 4 \times 10^3$, and $128 \leq \mathrm{Re} \leq 1.3087 \times 10^4$ are used to derive the correlation, which is a best fit with $R^2 = 0.9818$.

Conversely, for the inertia-less regime, $\Delta p_{3D}$ is better described by

$$\Delta p_{\mathrm{W,I}} = 0.2103 + 2.8549\ \mathrm{Ha}^{-1/2} \tag{5}$$

where 4 data points in the range $10 \leq \mathrm{N}\,/\,\mathrm{Ha}^{3/2} \leq 31.63$, $100 \leq \mathrm{Ha} \leq 1 \times 10^3$ and $\mathrm{Re} = 1$ are best fitted with $R^2 = 0.9585$.

Equations (4) and (5) are reasonably accurate if used to predict the numerical $\Delta p_{3D}$ calculated for the respective regimes, as shown in Figure 9b. The constant term in Equations (4) and (5) refers to the inertia-less/inviscid pressure loss, $\Delta p_\infty$, which is recovered for $\mathrm{N}, \mathrm{Ha} \to \infty$, as defined by Bühler et al. in [24]. It stands to reason that this term should be equal in both relations, but there is about a 5.65% discrepancy for $\Delta p_\infty$ between Equations (4) and (5). This could be explained with the onset of a transitional regime in some of the simulations used to derive Equation (4), in which $\mathrm{N}\,/\,\mathrm{Ha}^{3/2}$ is close to unity, and, therefore, $\Delta p_\infty$ in Equation (5) should be considered as a more reliable value for the head loss in the ideal condition of negligible inertial and viscous effects.

For an inertia-less/inviscid sudden expansion with $Z = 4$ and $c = 0.028$, Bühler et al. reported $\Delta p_\infty = 0.315$, which is about 50% higher than the one predicted by Equation (5). This is surprising since an higher value would

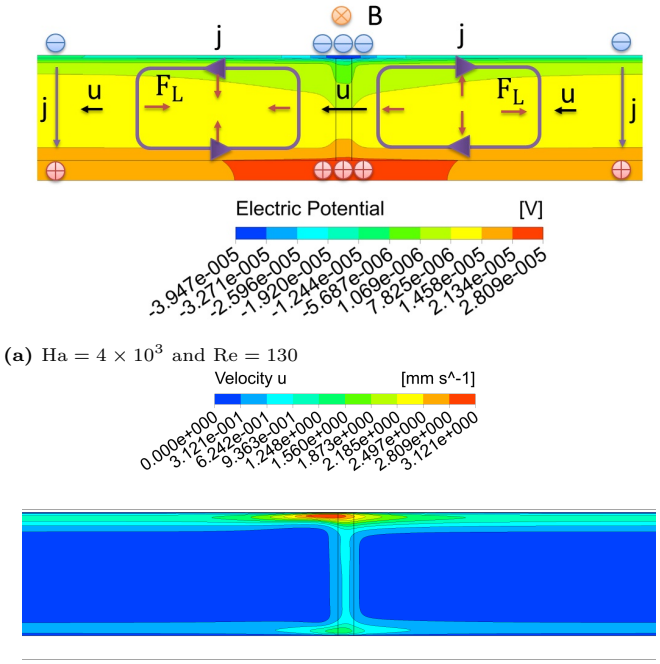


**(a)** Ha = $4 \times 10^3$ and Re = 130

**(b)** Ha = 500 and Re = 130

**Figure 7:** Electric potential distribution and qualitative description of current pattern and 3D Lorentz forces ($F_L$) for the flow through the interface (top), 3D MHD flow velocity (bottom). Data plotted on a radial-poloidal plane passing through the window center (z = 53 mm).

be expected from the concomitant sudden expansion and contraction due to the passage in the window. However, it is conceivable to explain this discrepancy due to the different geometry considered in the two studies. In Ref. [24], the sudden expansion is symmetrical around the duct axis, whereas the window position in our model forces the fluid expansion to be practically one-sided. Correspondingly, the effective cross-section variation is approximately 43% of that featured in Ref. [24]. The influence on the pressure loss of the window offset from the duct center-line is going to be addressed in a future study.

Considering $u_0$ and $B_0$ as previously defined, it is calculated that in the WCLL TBM there are $\mathrm{Ha} = 8 \times 10^3$ and $\mathrm{N} = 4.63 \times 10^5$. Therefore, a transitional regime can be expected in the inlet window since $\mathrm{N}\,/\,\mathrm{Ha}^{3/2} \approx 0.7$. Equation (4) is found to perform well for $\mathrm{N}\,/\,\mathrm{Ha}^{3/2} < 1$, whereas Equation (5) is preferred for $\mathrm{N}\,/\,\mathrm{Ha}^{3/2} \geq 1$.

For moderate change ratio ($Z \leq 4$), it is reasonable to assume that $\Delta p_{W,j}$ is a linear function of $Z$ [25] and, thus, the characteristic value for the outlet window ($\Delta p_{W,O}$) can be easily extrapolated from the inlet window value, cfr. Equations (4) and (5), so that

$$\Delta p_{W,O} = \frac{Z_O}{Z_I} \Delta p_{W,I} \approx 0.665 \Delta p_{W,I}. \tag{6}$$

Therefore, the total loss due to the interface between man-

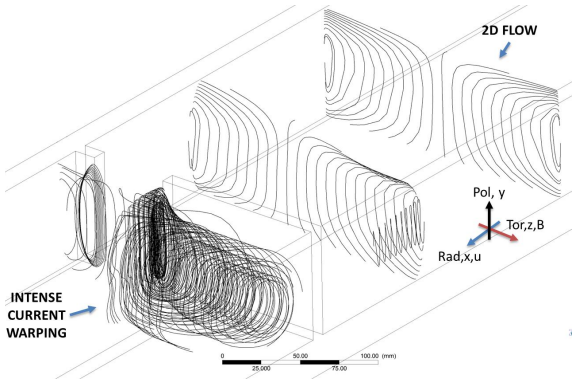


**(a)** Ha = 100

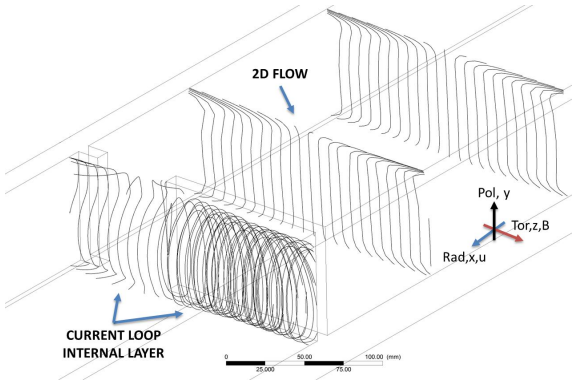


**(b)** Ha = $4 \times 10^3$

**Figure 8:** Current streamlines sampled on poloidal-toroidal planes downstream (x = 15 mm), upstream (x = -110 mm) and far upstream (x = -250 mm) of the window. Data refer to Re = 130.

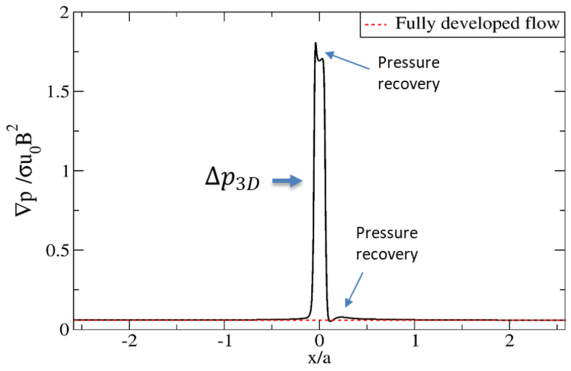


**(a)** Calculation methodology for $\Delta p_{3D}$, data shown for Ha = $4 \times 10^3$, Re = 130.

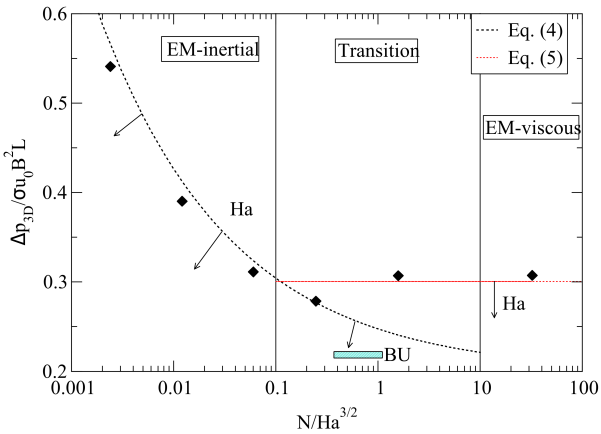


**(b)** $\Delta p_{3D}$ trend against flow regime at Ha = 1000.

**Figure 9:** Three-dimensional pressure loss analysis: (a) calculation methodology and (b) trend with flow regime. Turquoise box identifies parameter range for TBM (Ha = 8000) and arrows mark the trend of $\Delta p_{3D}$ for increasing Ha.

ifold and breeding zone is calculated simply as

$$\Delta p_{\mathrm{W}} = \Delta p_{\mathrm{W,I}} + \Delta p_{\mathrm{W,O}} \approx 1.665 \Delta p_{\mathrm{W,I}}. \qquad (7)$$

## 5. Fully developed flow

The flow is in fully developed state throughout most of the BZ (development length $l \approx a$, about 25% of the inlet duct, discounting the bend) and, therefore, it is of fundamental importance to correctly predict $\Delta p_{2D}$ or, equivalently, the pressure coefficient $\mathrm{k_p} = \nabla p\, a/p_0$. Since MHD flow in rectangular ducts is well understood, the study has been focused on the peculiarities that set apart the TBM design from a simple channel layout and can potentially alter the pressure drop.

### *5.1. Uneven wall thickness*

The BU radial channel is generally composed by two pairs of walls of unequal thickness that, in turn, corresponds to a similarly uneven equivalent conductivity, expressed through $\mathrm{c_{w,i}} = \sigma_w a/\sigma t_i$. Referring to the inlet (bottom) duct shown in Figure 3, the bottom and left wall are characterized by $t_i = t_w$ (which corresponds to $c_w = 0.2$), the thin plate separating the two ducts by $t_i = t_b$ ($c_b$=0.027), whereas the right wall, representative of the TBM side cap, features $t_i = t_c = 5/3 t_w$ (cfr. Table 2). Current pattern is bound to diverge from the behavior observed in a uniform conductivity duct, since currents will tend to close through more conductive walls, and this causes the alteration of flow features and $\mathrm{k_p}$. The analysis has been focused on the inlet (bottom) duct, hereafter referred as "B". Results are easily extrapolated to the outlet (top, "T") duct, where the only difference is the channel aspect ratio.

The thin (and thus poorly conducting) baffle plate that divides the two ducts, highlighted in Figure 3a, promotes a faster jet close to it compared with the opposite wall in Figure 10. In Figure 11, the numerical $\mathrm{k_p}$, indicated by the filled triangle symbols, and the analytical value, $k_0 = 9.97 \times 10^{-2}$, calculated for a uniform conductivity duct with $\mathrm{c_w} = \mathrm{c_{w,max}} = 0.2$ [5], are compared; the former is consistently below the latter. This is obviously caused by the increased current path resistivity through the thin plate, which curtails the Lorentz force intensity and, in turn, $\mathrm{k_p}$. It should be noted that our results overestimate the value predicted by an analytical relation that takes into account differential wall conductivity ($k_1 = 4.28 \times 10^{-2}$), even if they appear to asymptotically approach it [31]. This

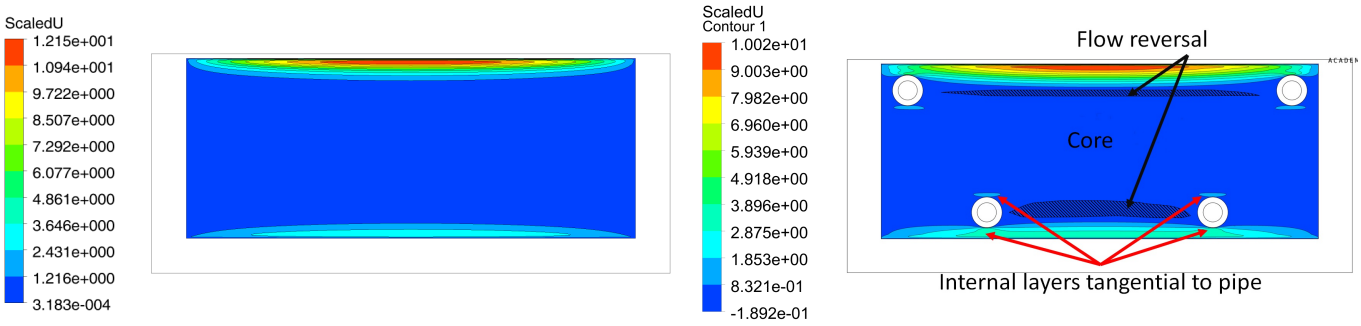


**Figure 10:** Dimension less velocity distribution ($u/u_0$) for fully developed flow in an inlet channel devoid of obstacles (left) and with cooling pipes, case "B-2" (right). Main flow features are marked for the latter. Data for Ha $= 2 \times 10^3$.

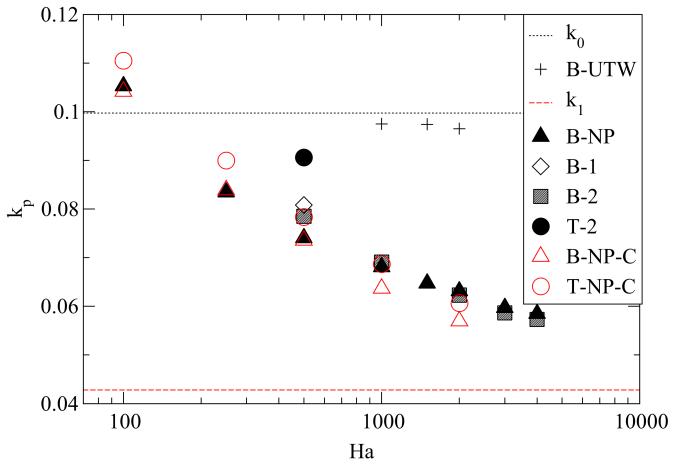


**Figure 11:** Fully developed flow dimensionless pressure gradient. Numerical results (symbols) are compared with the analytical value (dashed lines) for uniform ($k_0$) and non-uniform wall thickness ($k_1$). The symbol "B" identifies a pressure gradient calculated for the bottom duct geometry, whereas "T" refers to a result obtained for the top channel. Trailing symbols further specify the pipe layout ("1" for the back configuration and "2" for the frontal one, cfr. Table 4) or their absence ("NP"), "C" highlights results featuring coupling effects, and "UTW" simulations performed with uniform wall thickness.

discrepancy may be caused by the assumptions made to derive the analytical relation which consider N, Ha $\to \infty$, as $\mathrm{k_p} \to k_1$ when Ha is increased. Assuming that for Ha $\to \infty$ we have $\mathrm{k_p} \approx k_1$, our 8 data points are well fitted ($R^2 = 0.9835$) by the following relation

$$\mathrm{k_p} = k_1 + k_2 \cdot \mathrm{Ha}^{-1/3} \tag{8}$$

where $k_2 = 0.2614$. This results is surprising, since $\mathrm{k_p}$ is usually independent by Ha when Ha $\gg 1$, and it is likely related to the uneven wall thickness since simulations performed with the same numerical model for the uniform wall thickness case ($\mathrm{c_w} = 0.2$, marked with B-UTW in Figure 11) show the expected trend and good agreement with the theoretical relation $k_0$. To the best of our knowledge, a similar result has not yet been reported in the literature, even if it should be noted that experimental studies addressing uneven wall thickness are very rare.

No effect on the pressure loss is observed due to $\mathrm{c_w}$ difference of the walls perpendicular to $B$. This can be explained with the Hartmann walls being relatively thick, i.e. they not satisfy the condition $t_w/a \ll 1$: $t_w/a = 0.155$ for the vSP and $t_w/a = 0.258$ for the side cap. In a thick wall, the bulk of currents still tends to flow close to the fluid/solid interface since it is the more convenient path, and, as a result, a non-null potential gradient develops in the wall thickness [1]. Due to this phenomenon, the side cap does not provide a current path significantly less resistant than the vSP and the pressure gradient is unchanged.

### *5.2. Obstacles aligned with stream-wise direction*

Each BU is refrigerated by two inserted U-pipes. These are characterized by a geometry varying along the radial coordinate, as shown in Figures 3a and 3b. The pipes occupy part of the duct cross-section, which is no longer available for the fluid passage. A blockage ratio is defined through the relation

$$\beta_i = \frac{A_O}{A} = \frac{n\pi(d/2)^2}{4ab_i}. \tag{9}$$

In Equation (9), $A_O$ is the total obstacle area calculated for $n$ bodies of circular cross-section (2 per U-pipe) with external diameter $d = 13.5$ mm, and $A$ is the channel area devoid of any obstructions. Outlet T channel poloidal half-height is $b_T = 54$ mm, the other geometrical parameters are consistent with those of the B duct collected in Table 2. Since $n = 4$, it is possible to calculate $\beta_B = 0.0382$ for the inlet duct and $\beta_T = 0.0274$ for the outlet one.

The effect of the cooling pipes on $\mathrm{k_p}$ is analyzed considering three typical pipe configurations. These cases correspond to the layout at the back (B-1) and front (B-2) of the B duct and at the front of the T one (T-2). Pipe configuration is symmetrical about the poloidal centreline and each pipe position in the duct is identified by the distance from adjacent toroidal and poloidal walls ($G_i$, shown in Figure 12, together with a detail of the computational grid adopted). Geometrical information about the three models are collected in Table 4.

Each pipe provides additional conductive surfaces for the current closure in its wall ($t_p = 2.75$ mm) and, consequently, modify the flow pattern. Salient features are

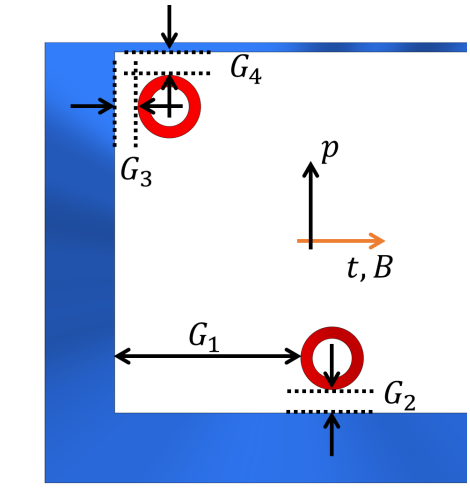


(a)

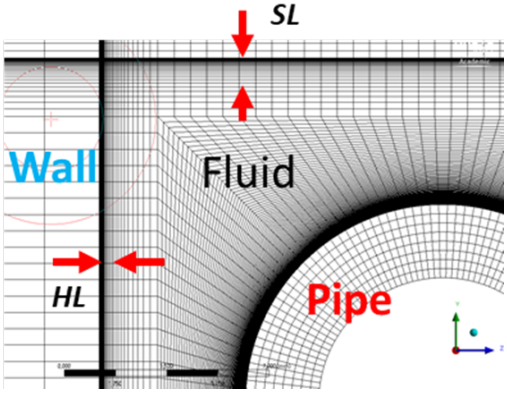


(b)

**Figure 12:** a: position of coolant pipes and distance from closest wall ($G_i$, cfr. Table 4) for the configuration B-2, only half channel is shown due to symmetry; b: detail of the computational mesh for the B-2 top pipe, thickness of Hartmann (HL) and Sidewall layer (SL) are highlighted.

presented for case B-2 in Figure 10; the other two configurations share a similar behavior. Internal layers are generated tangent to the pipe surface and spread along magnetic field lines, splitting the core into separate sub-regions. Reverse flow up to 1.5% of the imposed flow rate (growing with Ha) is observed in the space between pipes located at the same height in the channel. Toroidal distance between the pipes is observed to influence the appearance of the reverse flow; closer pipe pairs feature it at lower Ha. Pipe layout shift causes reorganization of the flow structures and, albeit being gradual, could trigger instabilities in the baffle jet.

The effect of the pipe on the current distribution is shown in Figure 13. The perturbed pattern is characterized by the appearance of saddle points that separate diverging current loops. If the pipe is close to the Hartmann wall, as it is the case for B-2, short-circuited loops appear between the two electrically conductive surfaces. The region between a pipe and the nearby Hartmann wall is in general characterized by a linear velocity profile matching the opposing Hartmann layers. The smaller distance

**Table 4:** Pipe system layout specifications expressed as tube distance from nearest set of walls, cfr. Figure 12a. Dimensions are expressed in mm. The symbol "B" refers to the bottom duct geometry, "T" to the top channel. Trailing symbols further specify the radial reference position: "1" is the layout close to the manifold interface and "2" close to the FW.

| | T-2 | B-2 | B-1 |
|---|---|---|---|
| $G_1$ | 40 | 40 | 30 |
| $G_2$ | 35 | 5 | 27.5 |
| $G_3$ | 5 | 5 | 30 |
| $G_4$ | 5 | 5 | 5 |

between those, the steeper the velocity gradient.

The obstacle effect on $k_p$ can be observed in Figure 11, where triangle and square symbols represent respectively a B duct empty and with cooling pipes. Pressure loss is increased at Ha $\leq 2 \times 10^3$ due to stronger viscous effects caused by the formation of additional Hartmann layers and higher mean velocity. At the same time, the relative low conductivity of the pipes reduces the Lorentz force intensity and, for Ha $> 2 \times 10^3$, it eventually overcomes the other effects and causes a slight $k_p$ reduction compared with the empty duct, as demonstrated in Figure 11.

Pipe effect on $k_p$ for case B-2 is estimated at $\pm 2\%$ and the 5 data points are best fitted by a relation mirroring Equation (8) and characterized by $R^2 = 0.9959$,

$$k_p = k_1 + k_3 \cdot \mathrm{Ha}^{-0.437} \tag{10}$$

with $k_3 = 0.542$. The pressure gradient calculated for case B-1 is consistent with B-2 which means that, as expected, pipe layout does not affect head loss for constant blockage ratio. An increase is indeed observed for case T-2, but it can be entirely explained with the channel aspect ratio since $k_p \propto b/a = \gamma$, and, indeed, $\gamma_B < \gamma_T$. Therefore, Equation (10) is suitable to predict the pipe effect on $k_p$, if the channel cross-section occupied by the cooling system is relatively small ($< 5\%$).

### *5.3. Electromagnetic coupling*

In the numerical model developed to study the MHD flow in the hairpin bend, discussed in Section 6, coupling effects appear between the adjacent B and T ducts. The two BU channels share three electrically conductive walls (the vSP, the side-cap and the in-BZ baffle plate shown in Figures 3a to 3c), which means that currents induced in one duct can close through the other, a phenomenon known as Madarame effect [1]. This can affect both flow features and pressure loss.

In the present case, we are dealing with two counter-flowing channels characterized by the same flow rate, moderate aspect ratio ($a/b > 1$), and stacked perpendicular to the magnetic field direction. The current distributions developing in the two channels are going to interact mainly through the thin, relatively wide, and poorly conductive baffle plate separating them (i.e. side wall coupling) [32].

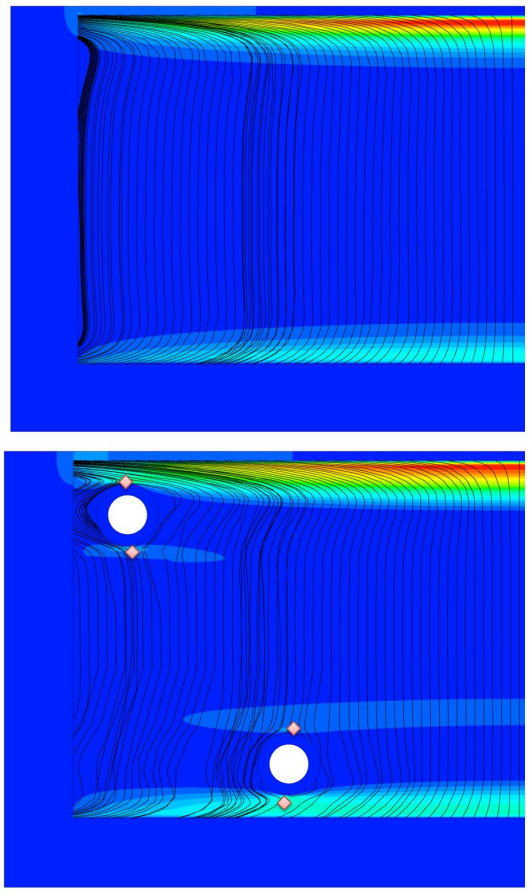

**Figure 13:** Electric potential gradient distribution and current streamlines for fully developed flow in an inlet channel devoid of obstacles (top) and with cooling pipes, case "B-2" (bottom). Diamonds mark the saddle points on the pipe surface separating diverging current loops. Data for Ha $= 2 \times 10^3$.

Since the two channels are connected at the bend and they are characterized by a similar mean velocity, no appreciable change is observed to develop in terms of flow features compared with the uncoupled case. This is illustrated in Figure 14 where the velocity profile in the B duct calculated for the 3D bend model, sampled across the side walls ($z = 0$) at approximately halfway of its radial extension ($x/a = 2$), is compared with the fully developed result obtained in the context of the study discussed in Section 5.2.

The coupling effect on the $k_p$ is presented in Figure 11. Filled and empty triangle symbols stand for the pressure loss in the B duct, respectively, in the absence and presence of coupling effects. The dimensionless pressure gradient is found to be reduced in the coupled duct by $\approx 10\%$ at Ha $= 2 \times 10^3$ between these two cases, the deviation progressively increasing with Ha and, conversely, coupling effect is found to be negligible for Ha $\leq 5 \times 10^2$. This can be explained with the currents induced in the two ducts sharing the baffle plate, which equivalent conductivity is further decreased, resulting in a diminished $k_p$.

Since no simulations have been performed for the T

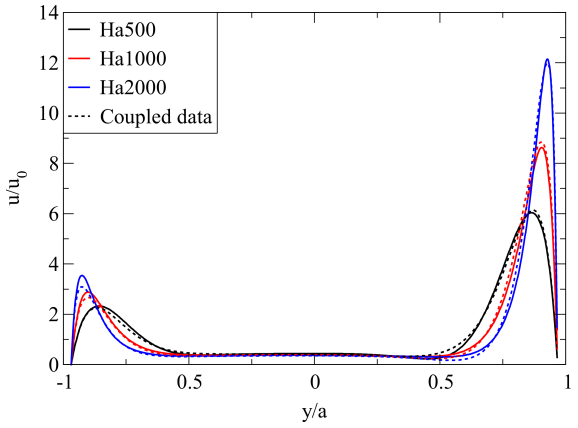


**Figure 14:** Thick lines mark the velocity profile across baffle (located at $y/a = 1$) and bottom SP ($y/a = -1$) in the bottom channel for no pipes and absence of coupling. Dashed lines refer to the velocity profile for the same channel, sampled at $x/a = 2$, in the presence of coupling with the top channel.

channel in the same conditions as B-NP, the effect of coupling on $k_p$ cannot be described quantitatively for this case. However, it can still be inferred from the results presented in Figure 11 that, assuming the pipe effect to be comparable to the B case, the coupling is reducing the pressure loss also for this case. This assumption is valid only if the pipe effect on pressure loss is independent from $\beta$, which is likely to be the case due to the low value associated to both B and T channel, and the duct aspect ratio. A more comprehensive parametric analysis for these two variables in a wider range than the one considered for this study should be performed to address this question.

It should be noted that coupling is not limited to the single BU composed by two channels that has been considered in this study but, rather, is a very complex phenomenon that links together in a non-trivial way all the BUs in the TBM. A full assessment of coupling effects on $k_p$ and flow features should be performed addressing them on the entire TBM module, which at the moment seems impractical due to the prohibitive computational cost. Nevertheless, motivation for such study are still pressing since TBM-scale coupling may result in an even larger depressing effect on pressure losses, as suggested by Zhang et al. [33], which will impact the Test Blanket System (TBS) operation. The presence of the poloidal magnetic field can further affect the coupling regime, as discussed in [34], with the poloidal field favoring the onset of reverse flow at the corner of the wall separating two counter-flowing channels, causing potential harmful consequences for tritium inventory control.

## 6. Hairpin bend with transverse obstacles

Close to the TBM FW, the breeder inverts its flow direction by executing a 180° turn. The magnetic field is perpendicular to the bend plane, therefore $\Delta p_{3D}$ is foreseen to be moderate compared with the opposite case of a flow turn occurring in the magnetic field plane [35]. The flow

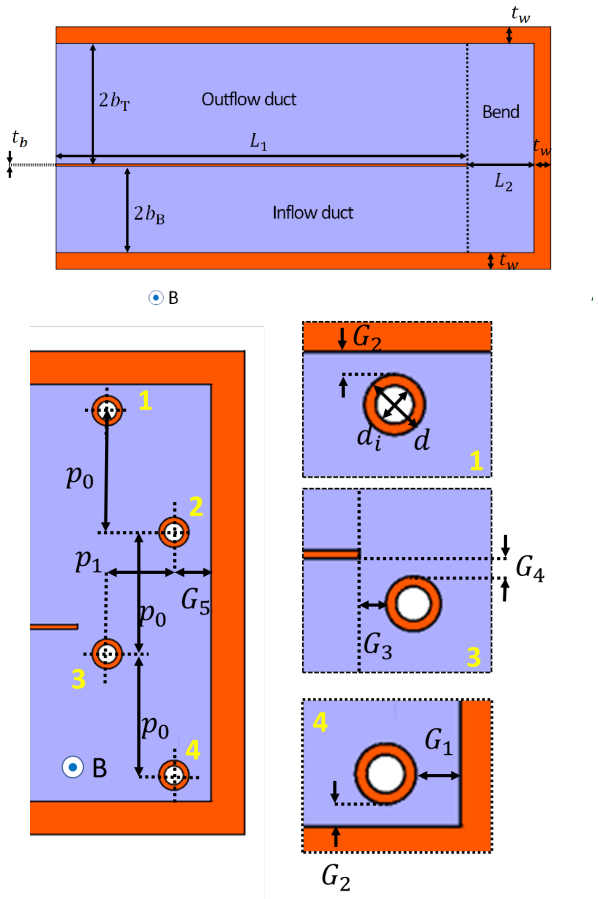


**Figure 15:** Geometry of the hairpin bend, radial-poloidal view (top). Bend region with transverse obstacles and detail of pipe placement (bottom). In purple the fluid domain, in orange the solid domain.

undergoes moderate cross-section variation, first from the inflow duct to the bend region and then from that to the outflow duct, that, being perpendicular to B, is assumed to give no significant contribution to $\Delta p_{3D}$. To simplify the model, the four U-pipes (two for each duct), described in Section 5.2, are considered as entirely transverse to the main flow direction and confined to the bend. Numerical model geometry is shown in Figure 15, whereas relevant parameter values are collected in Table 5. The blockage ratio for this configuration is difficult to define but, considering the radial-toroidal cross-section, for which only one pipe is present at any given poloidal height, it is possible to calculate $\beta = d/L_2 = 0.225$.

Two numerical models have been realized: one without any obstacles and the second including the transverse pipes. The latter has been found to be considerably more expensive to simulate, featuring approximately 3 times the element count compared with the former. For the simple hairpin bend, simulations have been performed in the range $0 \leq \mathrm{Ha} \leq 2 \times 10^3$ and $12 \leq \mathrm{Re} \leq 1.25 \times 10^3$. For the bend with obstacles, the investigation domain has been restricted to $0 \leq \mathrm{Ha} \leq 5 \times 10^2$ and $1 \leq \mathrm{Re} \leq 1.3 \times 10^2$.

The 3D MHD flow in the hairpin bend is presented

**Table 5:** Geometrical parameters for bend model, values are reported in mm.

| | | |
|---|---|---|
| Baffle plate radial length | $L_1 \approx 4a$ | 371 |
| Bend radial length | $L_2$ | 60 |
| Poloidal pipe pitch | $p_0$ | 54.7 |
| Radial pipe pitch | $p_1$ | 30 |
| Pipe distance from the wall | $G_1$ | 10 |
| | $G_2$ | 5 |
| | $G_3$ | 6.25 |
| | $G_4$ | 5 |
| | $G_5$ | 16.75 |

in Figure 16. The change of stream direction induces an electrical potential difference that, in turn, modifies the current distribution and causes additional losses with a similar mechanism as the one described in Section 4.2. The transition in the current pattern is evident in Figure 16. The fully developed flow in the radial channel is characterized by perfectly vertical (i.e. limited to the flow cross-section) current streamlines. As the flow approaches the bend, $J_x$ grows and the streamlines warp until they are nearly horizontal in the central section of the turn. Even at $\mathrm{Ha} = 100$, flow separation at the hSP/FW corners is completely suppressed, whereas the recirculation bubble at the baffle plate tip persists throughout the Ha range investigated, albeit significantly reduced [23]. Effect of transverse pipes on flow features is minor and substantially aligned with what observed in Section 5.2. Internal layers, characterized by local velocity overshoot, develop tangential to the pipe surface and parallel to the field (note A in Figure 16). The presence of the pipes causes small perturbations in the electric potential distribution due to the additional electrically conductive surface. This is particularly evident for pipe No. 3 (cfr. Figure 15), the closest one to the baffle plate, which internal layer interacts with the strong jet there and slightly perturbs the baffle recirculation bubble (note B in Figure 16). As it is discussed in Section 6.1, these changes in the flow features are not accompanied by a significant effect on the pressure loss.

The $\Delta p_{3D} = \Delta p_b$ is defined as the pressure loss occurring in the bend region, marked in Figures 3a and 3b, everywhere else the flow is in fully developed conditions. It can be calculated by estimating the $\Delta p_{2D}$ through the relation

$$\Delta p_{2D} = \frac{L_1}{a} \cdot \left( \mathrm{k}_{p,1} + \mathrm{k}_{p,2} \frac{b_B}{b_T} \right). \tag{11}$$

In Equation (11), $\mathrm{k}_{p,1}$ and $\mathrm{k}_{p,2}$ are the pressure coefficient for the inflow and outflow duct accounting for coupling effects, but in absence of pipe, which are graphically presented in Figure 11 and tabulated in Table 6. It is straightforward to observe that, by definition, we have $\Delta p_b = \Delta p - \Delta p_{2D}$, in which $\Delta p$ is the total loss calculated in the model (see Figure 17a).

Contributions to $\Delta p_b$ can be expected from both the

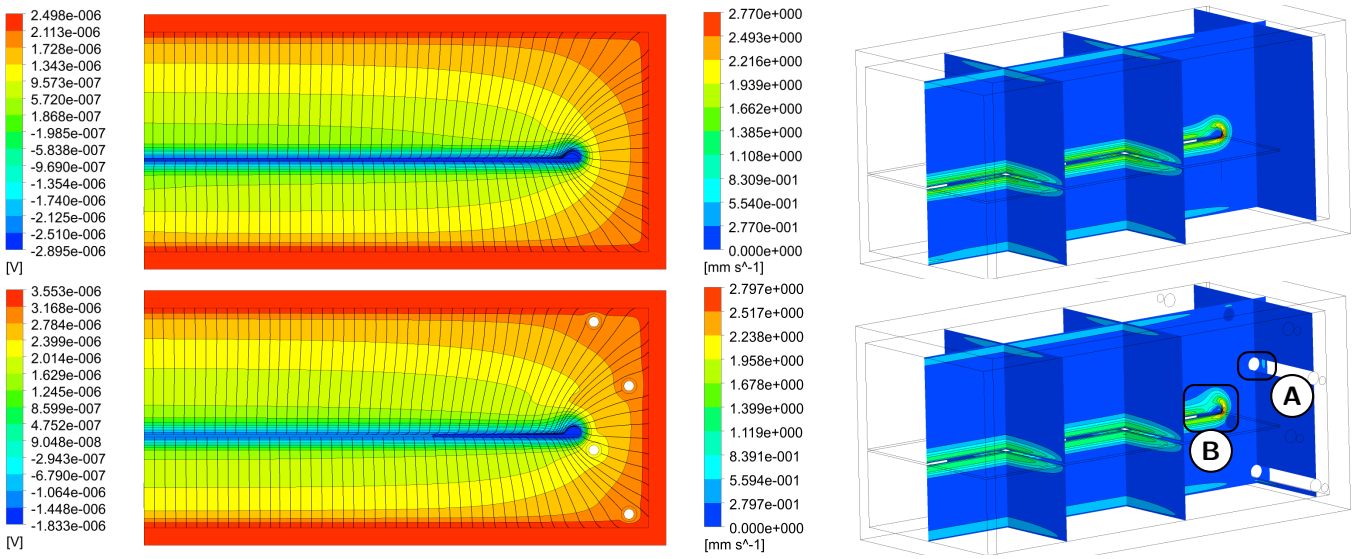


**Figure 16:** Electric potential and current streamlines (left) on the central radial-poloidal plane ($z = 0$ mm) compared for the bend with and without cooling pipes (bottom/top). Velocity distribution sampled on the same plane and three toroidal-poloidal planes at $x = 100$mm, 250 mm, and 415 mm is shown on the right. Development of jet in internal layer tangential to pipe surface and aligned to field (A) and flow separation at baffle plate tip (B). Data refer to Ha = 500 and Re = 130.

**Table 6:** Pressure coefficient in inflow ($k_{p,B}$) and outflow ($k_{p,T}$) duct accounting for coupling and non-uniform wall conductivity effects.

| Ha | $k_{p,B}$ | $k_{p,T}$ |
|---|---|---|
| 100 | 0.10418 | 0.07928 |
| 250 | 0.08391 | 0.06456 |
| 500 | 0.07354 | 0.05624 |
| 1000 | 0.06368 | 0.04928 |
| 2000 | 0.05696 | 0.04354 |

stream direction change and presence of cooling pipes. These contributions are, in general, $f(\mathrm{Ha}, \mathrm{N})$. It is observed that, in absence of obstacles, $\Delta p_b \approx 10\% \Delta p$, and that $\Delta p_b$ is constant for $\mathrm{Ha} \geq 1 \times 10^3$ (Figure 17b). Data obtained for $\overline{u} = u_0$ are best fitted by the relation

$$\Delta p_\mathrm{b} = 0.0466 + 63.306\,\mathrm{Ha}^{-3/2}, \tag{12}$$

which has been obtained with 5 data points in the range $100 \leq \mathrm{Ha} \leq 2 \times 10^3$ and Re = 130, best fitted by Equation (12) with $R^2 = 0.9506$. Equation (12) suggests that inertial effects are important in the estimate of $\Delta p_\mathrm{b}$ at low Ha and moderate N, but they quickly become negligible if $\mathrm{N} > 2 \times 10^3$.

A comprehensive evaluation of inertial effects, like the one performed in Section 4, has not been carried on for the bend due to time limitation. Simulations at $\overline{u}_{min} = 0.1u_0$ and $\overline{u}_{max} = 10u_0$ have been executed to provide an indication about the lower and upper boundary for $\Delta p_b$ in a wider velocity range centered on the current foreseen flow rate for the WCLL TBM. It has been observed that $\Delta p_b(\overline{u}_{min}) \approx \Delta p_b(u_0)$, whereas a noticeable increase in the three-dimensional pressure was found for $\Delta p_b(\overline{u}_{max}) \approx 1.5\Delta p_b(u_0)$. These results hint to a negligible influence of the inertial effects for $\Delta p_b$ unless a flow rate much higher than the one currently considered for the TBM is chosen as reference for nominal operation. Therefore, it seems reasonable to use Equation (12) to approximate its contribution to the total BU pressure loss.

It is interesting to compare the current numerical results with other one found in the literature. For a parallel hairpin bend in the inertia-less regime, the 3D pressure loss can be estimated using the relation derived by Reimann et al. for a 90° bend in a square duct [36]

$$k_R = q\frac{\mathrm{c_w}}{\mathrm{c_w} + 4/3} \cdot m, \tag{13}$$

where it is assumed that $m = 2$, i.e. that the pressure coefficient in two successive 90° bend can be confounded with the one for a 180° turn, an assumption that is justified if inertial effects are negligible, and $q = 1.063$ is a constant coefficient determined experimentally. According to Equation (13), it is found that $k_R = 0.2773$ for $c_w = 0.2$. To obtain the pressure coefficient $k$ for the simulated hairpin bend, it is necessary to convert the dimensionless 3D loss. The dimensional 3D pressure loss can be expressed as

$$\Delta p^*_{3D} = \frac{1}{2} k^* p_0. \tag{14}$$

Since $\Delta p_b = \Delta p^*_{3D}/p_0$, it is straightforward to derive from Equation (12) that, for $\mathrm{Ha} \to \infty$, $k^* = 2\Delta p_b = 9.32 \times 10^{-2}$. Therefore, $k^* \approx k_R/3$, which confirms that pressure loss due to 3D effects in a perpendicular bend are less intense than for an analogous geometry with a parallel magnetic field. Interestingly, this relationship is the same that has been assumed by the authors in Ref. [5].

It should be noted that Equation (13) is formally valid only for a square duct ($a/b = 1$), as it is evident from the

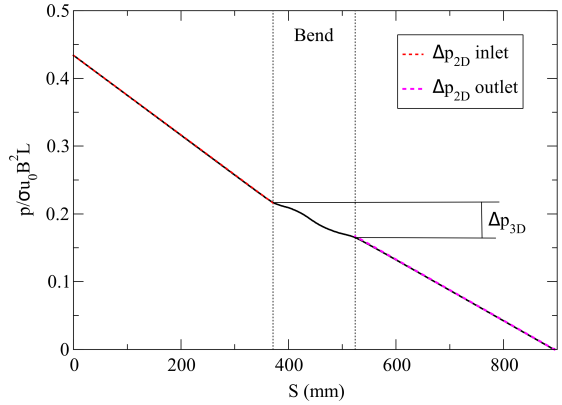


**(a)** Calculation methodology for $\Delta p_{3D} = \Delta p_b$.

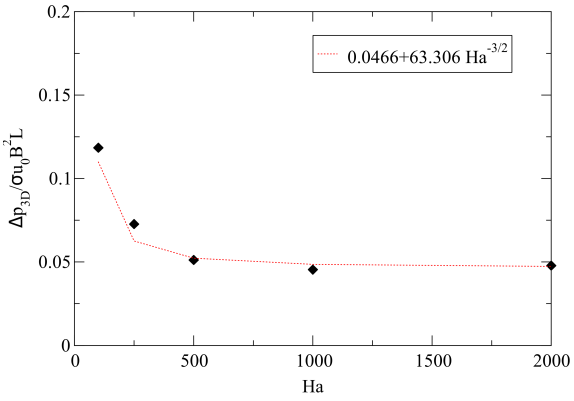


**(b)** $\Delta p_{3D} = \Delta p_b$ trend with Ha.

**Figure 17:** Bend $\Delta p_{3D} = \Delta p_b$ estimate at $\overline{u} = u_0$.

factor 4/3 present at the denominator of the right-hand term. This is derived by the general formula of $k_p$ for the fully developed flow in a rectangular duct with electrically conductive wall [31, 37], which can be written as

$$k_p = \frac{c_w}{c_w + 1 + a/3b} \tag{15}$$

If $a/b = 1$, Equation (15) is identical to the group in Equation (13), i.e. $c_w/(c_w + 4/3)$. Assuming that $\Delta p_{3D}$ in a bend has the same general trend of $k_p$ with regard to the aspect ratio, so that we can consider $q$ = const., Equation (13) can be generalized by substituting Equation (15) in lieu of the simplified group

$$k_R\prime = q\, k_p \cdot m. \tag{16}$$

For the present case, we can consider the average aspect ratio of the two radial channels as characterizing the hairpin bend

$$\gamma = \frac{a/b_B + a/b_T}{2} = \frac{a}{2b_B}\left(\frac{b_B + b_T}{b_T}\right) \tag{17}$$

where from the data in Table 2, it follows that $\gamma = 2.144$ and $k_R\prime = 0.1271$ with $k_R/k_R\prime \approx 2.181$. The revised Reimann coefficient is significantly lower and quite close to the one calculated numerically, so that $k_R\prime/k^* \approx 1.364$.

This result is in apparent contradiction with the consensus that change of stream direction in a plane perpendicular to the magnetic field is very less loss-intensive than one that is instead coplanar. A possible explanation is that $q$ is not constant but rather that $q = f(\gamma)$. Morevoer, it is possible that $k^*$ is partially inflated by the change in cross-section between the bottom and top channel that, even if quite small, is a separate contribution that is impossible to discern in the current formulation from the "pure" bend loss as defined in Equations (13) and (16). Finally, the effect of uneven wall conductivity on $k^*$ should also be considered. Clearly, a more in-depth parametric analysis for $\gamma$ and $c_b$ or, ideally, experimental data obtained for different hairpin bend configurations, could clarify this point.

### *6.1. Effect of cooling pipes on pressure loss*

Cooling pipes in the bend reduce available cross-section for the fluid movement and introduce additional paths for current closure, as discussed in Section 5.2. These effects increase $\Delta p_b$ by about 15% for the range Ha = [100, 500]. However, this contribution is negligible when accounted for the effect on $\Delta p$, where the obstacle penalty is estimated at $\approx 1\%$ for Ha = 500 and decreasing with Ha. In light of this, inertial effects on obstacle penalty can be assumed to be negligible as well. The pressure loss due to the 4 obstacles can be estimated with the value

$$\Delta p_O = 8.18 \times 10^{-3}, \tag{18}$$

thus, that the total additional loss in the bend is $\Delta p_b' = \Delta p_b + \Delta p_O$. For practical purposes, $\Delta p_b' \approx \Delta p_b$.

It is interesting to compare the numerical results with the estimate of a 3D pressure loss introduced by a pipe transverse to the main stream direction and aligned with the magnetic field that can be obtained using the correlation proposed by the authors in Refs. [5, 38, 39]. The obstacle dimensionless pressure loss for the pipe assembly is expressed by the relation

$$\Delta p_O^+ = n\frac{d}{2a}k^+ B^{g-2}. \tag{19}$$

In Equation (19), the constants are taken as $k^+ = 0.1931$ and $g = 1.73$, whereas $n = 4$ is the number of transverse pipes. At Ha = 500 (B=0.25T), Equation (19) gives a $\Delta p_O^+ = 7.84 \times 10^{-2}$, which is nearly ten times the code estimate $\Delta p_O$. This significant overestimate seems to hint to the conclusion that Equation (19) could be unsuitable to predict the pressure loss due to the particular pipe geometry considered in the WCLL TBM.

## 7. Estimate of total pressure loss

From the outcome of the discussed analyses, it is possible to estimate the overall $\Delta p_t$ in the BZ from Equations (4) and (12) and the $\Delta p_{2D}$ from Equation (11), derived capping $k_{p.1}$ and $k_{p.2}$ at the value calculated for Ha $=2 \times 10^3$

(cfr. Figure 11 and Table 6). We neglect the pipe effect on the pressure loss since it does not significantly affect the overall estimate, as demonstrated in Sections 5.2 and 6. It follows that

$$\Delta p_t(\mathrm{Ha}, \mathrm{N}) = 1.665\Delta p_{\mathrm{W,I}} + \Delta p_{\mathrm{b}} + \Delta p_{2D} \qquad (20)$$

where $L_1/a \approx 3.83$ and $b_B/b_T = 0.7176$ in $\Delta p_{2D}$ from Equation (11). For $\mathrm{Ha} = 8 \times 10^3$ and $\mathrm{N} = 4.63 \times 10^5$, $\Delta p_t = 0.7486$. In dimensional form, this corresponds to $\Delta p_0 p_t = 2.414 \times 10^2$ Pa. Equation (20) can easily by employed to estimate the pressure loss at different values of mean velocity and applied magnetic field.

### *7.1. Uncertainty*

Relevant simplifications are introduced during the performing of computational analyses. These assumptions will cause uncertainties in the MHD pressure loss estimate obtained from Equation (20) that, in principle, could deviate from the actual behavior of the WCLL TBM, even significantly. The most important of these assumptions are listed below:

1. Unidirectional toroidal field ($B \approx B_t$) in lieu of a more realistic treatment including the poloidal contribution, i.e. $B_p \approx B_t/3$ [7]
2. Large-scale coupling effects between neighboring BUs, see also the previous point (cfr. [34])
3. Geometrical simplification of the BZ/manifold interface (obstacle presence, main poloidal flow, change of direction)
4. Buoyancy phenomena emerging due to the interaction of volumetric heating and cooling pipes are neglected

#### *7.1.1. Inclined field*

Regarding $B_p$, the presence of a bi-directional magnetic field could affect, in principle, both the fully developed pressure gradient and three-dimensional losses. The effect of a skewed magnetic field on the pressure loss for a fully developed flow in a rectangular duct was first observed experimentally by Alty [40] and recent numerical analyses addressing this topic can be found in Refs. [38, 41, 42]. The skewed field causes a flow rearrangement due to the modification of the current distribution on the duct cross-section with the formation of distinct core regions separated by internal layers, which are originated at corners or other geometry singularity points and propagate along the field lines. Similarly, the pressure gradient deviates from its unidirectional flow value by an amount which is dependent on the field inclination ($\alpha$), $\mathrm{c_w}$, Ha, and aspect ratio ($a/b$). For the WCLL TBM, the average field inclination to be expected on the toroidal direction can be calculated as $\alpha = \arctan(B_p/B_t) \approx 18.5^\circ$. Assuming that the maximum variation of the poloidal field during the reactor operation does not exceed $\pm 50\%$ of its nominal value [43], it follows that $\alpha = 18.5^\circ \pm 7.5^\circ$.

For this range of magnetic field inclination, Zhang et al. observed a limited change in the pressure gradient compared with the case of purely toroidal field for a duct with uniform wall conductivity ($\mathrm{c_w}$=$1 \times 10^{-2}$), $1 \leq a/b \leq 2$ and $\mathrm{Ha} = 2 \times 10^3$: for the limiting case of a square duct ($a/b = 1$), $\nabla p(\alpha = 24^\circ)/\nabla p(0^\circ) = 0.95$, whereas for $a/b = 2$ it was found that $\nabla p(24^\circ)/\nabla p(0^\circ) = 1.05$ [41]. Even allowing for a stronger penalty on the pressure gradient for Ha and $\mathrm{c_w}$ closer to the WCLL TBM, which was observed by Zhang et al., the effect of the skewed field on the fully developed pressure loss will most likely be moderate.

However, the effect of uneven wall thickness should not be discounted since it is another factor that is affecting the current distribution and can interact with the secondary field. For a duct with a wall configuration closer to the WCLL TBM one but higher aspect ratio ($a/b = 4$), i.e. one poorly conducting side wall and the other three walls characterized by a similar $\mathrm{c_w}$, Tassone et al. observed that $\nabla p(16^\circ) \approx \nabla p(0^\circ)$ and that, in the range $0^\circ \leq \alpha \leq 24^\circ$, $0.9 \leq \nabla p(\alpha)/\nabla p(16^\circ) \leq 1.25$ [38]. Conduits with smaller $a/b$ tend to feature a similarly smaller $\nabla p(\alpha)$ but, since those results were obtained at $Ha \approx 100$, it is conceivable that a significant deviation for $\Delta p_{2D}$ could be observed compared with the present estimate.

The effect of the skewed field on three-dimensional pressure drop is less studied in the literature but it operates through similar mechanisms as those described for the fully developed flow. For the case of a fringing magnetic field in a rectangular duct, Zhang et al. found that $\Delta p_{3D}(22.5^\circ) \approx 2\Delta p_{3D}(0^\circ)$. The three-dimensional pressure drop caused by a cross-section variation due to a transverse obstacle was studied by Tassone et al. In that case, the inclined field had a depressing effect with $0.917 \leq \Delta p_{3D}(\alpha)/\Delta p_{3D}(0^\circ) \leq 0.99$ in the range $0^\circ \leq \alpha \leq 24^\circ$ [38]. To the best of our knowledge, no similar studies addressing sudden cross-section variation or change of stream-direction have yet been reported in the literature; a behavior similar to the one reported in Ref. [41] could be taken as a preliminary indication for the $\Delta p_{W,I}$ and $\Delta p_b$ uncertainty upper boundary.

#### *7.1.2. Coupling*

Coupling effects on the pressure loss, especially at large-scale, are strongly dependent on the configuration considered and are quite difficult to estimate. Counter-flowing channels from nearby BUs could potentially further reduce $\Delta p_{2D}$ compared with the simple case considered in Section 5.3, as well as coupling via Hartmann wall with the neighboring BU stack. For this last case, the flow in co-flowing square channels has been theoretically investigated by Bluck et al. [44] and numerically by Zhang et al. [45]. In particular, the latter investigated this effect alongside an inclined magnetic field and observed $\approx$15% pressure gradient decrease for $\alpha \approx 22^\circ$, $\mathrm{c_w} = 0.1$ and $\mathrm{Ha} = 1 \times 10^3$ compared with the purely toroidal field case [45].

#### *7.1.3. Simplification of BZ/manifold interface*

In the estimate of the pressure loss at the BZ/manifold interface, it has been chosen to reduce this hydraulic element to its dominant feature, the sudden cross-section

variation through an orifice. In the numerical model described in Section 4, the flow is assumed to be purely radial in nature and fully developed, thus neglecting the poloidal flow occurring in the manifold and the change of stream direction necessary for the LM to enter the orifice in the first place. This simplification drastically changes the nature of the MHD flow upstream of the orifice and, in turn, of the three-dimensional current distribution, whereas downstream it is consistent with the BU geometry. Moreover, the flow rate passing through the orifice is imposed assuming uniform flow distribution across all the BUs, which is not necessarily the case due to coupling effects, as discussed in Ref. [4]. The poloidal-to-radial change in stream direction executed in the manifold can be approximated with a 90° sharp bend which is, in principle, similar to the case discussed in Section 6 and, being perpendicular to the applied magnetic field, is expected to be a relatively small contribution to the pressure loss [5, 31]. A full three-dimensional analysis with a more realistic manifold geometry would be required to confirm this argument and assess if the effect on the pressure loss from this hydraulic element could be evaluated through the relation obtained for a 90° sharp bend.

*7.1.4. Magneto-convective phenomena*

Volumetric heating in the BU creates strong temperature gradients in the radial direction that will cause the onset of magneto-convective phenomena. These can affect the flow features by modifying the velocity profile and provoking instabilities, even at the high magnetic field expected in fusion reactors [46]. Recent numerical analyses dealing with this aspect in a geometry close to the WCLL TBM can be found in Ref. [47, 48]. The flow pattern is dominated by the strong upward buoyancy forces arising close to the FW and their interaction with the downward movement promoted by the cooling pipes. Large scale vortical-structures are observed in the bend region and mostly disjointed from the flow in the main radial channels that, conversely, is found to be unperturbed [47, 48]. Although important for flow characterization, heat and mass transport, these phenomena are expected to not affect by a significant degree the pressure loss estimate. It is likely that the upward lift in the bend region could cause a minor decrease in the total pressure loss, but this has yet to be confirmed in the literature.

## 8. Conclusions

The MHD flow in the WCLL TBM BZ has been analyzed through direct numerical simulation and a scaling law has been derived, Equation (20), to allow a quick estimate of its pressure loss depending on reference parameters. This study focused on hydraulic elements that are peculiar to the WCLL TBM:

- Sudden asymmetric contraction/expansion at the BZ/manifold interface
- Uneven wall thickness and equivalent conductivity ($c_w$)
- Fully developed flow around stream-wise aligned cooling pipes
- Electromagnetic coupling between counter-flowing channels
- Hairpin bend with presence of transverse obstacles

Uncertainty in the pressure loss estimate due to the model assumptions are briefly discussed in Section 7.1. The detailed flow characterization of the analyzed hydraulic elements is of interest for the TBM design for reasons other than the pressure loss, i.e. tritium control and corrosion, but it has not been possible to discuss it here extensively due to space reason. However, it will be the subject of a forthcoming paper.

The main head loss in the TBM is from the inlet and outlet windows that, together, accounts for 48.5% of the total. Gradual cross-section variation should be preferred to reduce it. The assumption that cross-section change is the main contribution to interface loss should be verified by future works including a more realistic geometry for the upstream area, ideally featuring a significant poloidal length of the manifold channel, as present in Ref. [4]. Secondarily, the effect of a bi-directional field on $\Delta p_{3D}$ should be investigated for the interface and the BU at large.

Cooling pipes do not affect significantly the pressure drop, either $\Delta p_{2D}$ or $\Delta p_{3D}$, but cause the formation of reverse flow spots when aligned with the stream direction that can promote tritium accumulation. It should be highlighted that the actual pipe layout in the BU is much more complex than the one considered in this study. For instance, transition between back and frontal pipe layout can hamper the reverse flow onset and affect the flow stability. A 3D MHD simulation of the BU including the complete pipe layout is desirable to investigate these aspects and a non-negotiable necessity to assess magneto-convective phenomena. This last topic is particularly relevant to obtain a reliable estimate of temperature distribution in the breeder [47, 48], necessary to comply with the structural material requirements, and mass transport phenomena [49]. Unfortunately, these detailed analyses are also associated to an exorbitant computational cost.

Finally, our study hinted that the fully developed dimensionless pressure gradient $k_p$ in a duct with uneven wall thickness may be dependent on Ha. This is a very surprising result since $k_p$ is usually independent by magnetic field intensity, its effect already included in the scale $p_0/a = \sigma u_0 B_0^2$, and it is not consistent with the theoretical solution developed by Tao and Ni [50], although this study had been developed for an Hunt flow with asymmetrical Hartmann walls. Since this behavior appears to be characteristic of a finite conductivity duct featuring a thin and poorly conductive sidewall surrounded by walls of higher

conductivity, it is possible that it has not been possible to detect it in Ref. [50]. This preliminary result should be confirmed by an additional study performing an extensive parametric analysis on duct with uneven wall thickness, ideally supported by theoretical work.

## CRediT authorship contribution statement

**Alessandro Tassone:** Conceptualization, Methodology, Investigation, Visualization, Writing - Original Draft. **Gianfranco Caruso:** Resources, Writing - Review & Editing.

## Acknowledgements

This work has been carried out within the framework of the EUROfusion Consortium and has received funding from the Euratom research and training programme 2014-2018 and 2019-2020 under grant agreement No 633053. The views and opinions expressed herein do not necessarily reflect those of the European Commission.

## References

[1] U. Müller, L. Bühler, Magnetofluiddynamics in channels and containers, Springer Science & Business Media, 2013.

[2] L. M. Giancarli, X. Bravo, S. Cho, M. Ferrari, T. Hayashi, B.-Y. Kim, A. Leal-Pereira, J.-P. Martins, M. Merola, R. Pascal, et al., Overview of recent ITER TBM Program activities, Fusion Engineering and Design 158 (2020) 111674. Doi: 10.1016/j.fusengdes.2020.111674.

[3] J. Aubert, G. Aiello, D. Alonso, T. Batal, R. Boullon, S. Burles, B. Cantone, F. Cismondi, A. Del Nevo, L. Maqueda, et al., Design and preliminary analyses of the new Water Cooled Lithium Lead TBM for ITER, Fusion Engineering and Design 160 (2020) 111921. Doi: 10.1016/j.fusengdes.2020.111921.

[4] C. Mistrangelo, L. Bühler, EFDA D 2NW59J, MHD Analyses for PBS 56.F1.TB – KIT Contribution, EUROfusion, 2020. Available online at: https://idm.euro-fusion.org/?uid=2NW59J.

[5] A. Tassone, G. Caruso, A. Del Nevo, Influence of PbLi hydraulic path and integration layout on MHD pressure losses, Fusion Engineering and Design 155 (2020) 111517. Doi: 10.1016/j.fusengdes.2020.111517.

[6] T. J. Dolan, R. W. Moir, W. Manheimer, L. C. Cadwallader, M. J. Neumann, Magnetic fusion technology, Springer, 2013.

[7] J. Vallory, Private communication, 2021.

[8] R. Boullon, J. Aubert, A. Morin, Definition of a WCLL reference TBM set design based on the WCLL BB design - First CAD model and scoping calculations, CEA, 2019. Available online for EUROfusion members at https://idm.euro-fusion.org/?uid=2N7CDT.

[9] D. Martelli, A. Venturini, M. Utili, Literature review of lead-lithium thermophysical properties, Fusion Engineering and Design 138 (2019) 183–195. Doi: 10.1016/j.fusengdes.2018.11.028.

[10] K. Mergia, N. Boukos, Structural, thermal, electrical and magnetic properties of Eurofer 97 steel, Journal of Nuclear Materials 373 (2008) 1–8. Doi: 10.1016/j.jnucmat.2007.03.267.

[11] L. Melchiorri, V. Narcisi, F. Giannetti, G. Caruso, A. Tassone, Development of a RELAP5/MOD3.3 module for MHD pressure drop analysis in liquid metals loops. Part I: Verification and Validation, 2021. In preparation.

[12] L. Melchiorri, V. Narcisi, F. Giannetti, G. Caruso, A. Tassone, Development of a RELAP5/MOD3.3 module for MHD pressure drop analysis in liquid metals loops. Part II: Application to the WCLL TBM, 2021. In preparation.

[13] M. J. Wolfendale, M. J. Bluck, A coupled systems code-CFD MHD solver for fusion blanket design, Fusion Engineering and Design 98 (2015) 1902–1906. doi:10.1016/j.fusengdes.2015.04.025.

[14] S. H. Kim, M. H. Kim, D. W. Lee, C. Choi, Code validation and development for MHD analysis of liquid metal flow in Korean TBM, Fusion Engineering and Design 87 (2012) 951–955.

[15] A. Froio, A. Batti, A. Del Nevo, L. Savoldi, A. Spagnuolo, R. Zanino, Implementation of a system-level magnetohydrodynamic model in the GETTHEM code for the analysis of the EU DEMO WCLL Breeding Blanket, in: American Nuclear Society (Ed.), Proceedings of TOFE 2020, Charleston, SC, 2020, pp. 1–6.

[16] A. Del Nevo, P. Arena, G. Caruso, P. Chiovaro, P. Di Maio, M. Eboli, F. Edemetti, N. Forgione, R. Forte, A. Froio, et al., Recent progress in developing a feasible and integrated conceptual design of the WCLL BB in EUROfusion project, Fusion Engineering and Design (2019). Doi: 10.1016/j.fusengdes.2019.03.040.

[17] I. Ricapito, PbLi flow-rate: selection of NOS value and operational domain, EUROfusion, 2020. Available online for EUROfusion members at https://idm.euro-fusion.org/?uid=2GDTP7.

[18] A. Tassone, S. Siriano, G. Caruso, M. Utili, A. Del Nevo, MHD pressure drop estimate for the WCLL in-magnet PbLi loop, Fusion Engineering and Design 160 (2020) 111830. Doi: 10.1016/j.fusengdes.2020.111830.

[19] ANSYS, Inc., CFX Solver Theory Guide, ANSYS, 2018.

[20] ANSYS, Inc., CFX Solver Modeling Guide, ANSYS, 2018.

[21] A. Tassone, Study on liquid metal magnetohydrodynamic flows and numerical application to a water-cooled blanket for fusion reactors, PhD thesis, Sapienza University of Rome, March 2019. Available online at: https://iris.uniroma1.it/retrieve/handle/11573/1243658/1054590/Tesi_dottorato_Tassone.pdf.

[22] S. Smolentsev, T. Rhodes, Y. Yan, A. Tassone, C. Mistrangelo, L. Bühler, F. Urgorri, Code-to-Code Comparison for a PbLi Mixed-Convection MHD Flow, Fusion Science and Technology (2020) 1–17. Doi: 10.1080/15361055.2020.1751378.

[23] A. Tassone, G. Caruso, PMI-7.1.1.Phase II - Task 4 Analys-T001-D002 (D10.2), EFDA D 2NQ8E5 ver. 1.1, Analysis results on the BZ MHD flow (MHD Analyses for PBS 56.F1.TB), Eurofusion, 2020. Available online for EUROfusion members at https://idm.euro-fusion.org/?uid=2NQ8E5.

[24] L. Bühler, S. Horanyi, Experimental investigation of MHD flows in sudden expansion, Forschungszentrum Karlsruhe, 2006. Tech. Rep. FZKA 7245.

[25] L. Bühler, A parametric study of 3d mhd flows in expansions of rectangular ducts, Fusion science and technology 52 (2007) 595–602. Doi: 10.13182/FST07-A1553.

[26] S. Molokov, Liquid metal flows in manifolds and expansions of insulating rectangular ducts in the plane perpendicular to a strong magnetic field, Forschungszentrum Karlsruhe, 1994. Tech. Rep. FZKA 5272.

[27] C. Mistrangelo, Three-dimensional MHD flow in sudden expansions, Forschungszentrum Karlsruhe, 2006. Tech. Rep. FZKA 7201.

[28] J. Hunt, S. Leibovich, Magnetohydrodynamic flow in channels of variable cross-section with strong transverse magnetic fields, Journal of Fluid Mechanics 28 (1967) 241–260. Doi: 10.1017/S0022112067002046.

[29] S. Y. Molokov, L. Bühler, R. Stieglitz, Asymptotic structure of magnetohydrodynamic flows in bends, Magnetohydrodynamics (0024-998X) 31 (1995) 357–366.

[30] S. Aleksandrova, S. Molokov, The structure of parallel layers in steady two-dimensional magnetohydrodynamic flows in sudden duct expansions and contractions, Theoretical and Computational Fluid Dynamics 26 (2012) 29–35. Doi:

10.1007/s00162-010-0212-8.

[31] I. R. Kirillov, C. B. Reed, L. Barleon, K. Miyazaki, Present understanding of MHD and heat transfer phenomena for liquid metal blankets, Fusion engineering and design 27 (1995) 553–569. Doi: 10.1016/0920-3796(95)90171-X.

[32] C. Mistrangelo, L. Bühler, Electro-magnetic flow coupling for liquid metal blanket applications, Fusion Engineering and Design 109 (2016) 1452–1457. Doi: 10.1016/j.fusengdes.2015.11.052.

[33] X. Zhang, C. Pan, Z. Xu, Investigation of coupling mhd rectangular ducts flows based on a fully developed modeling, IEEE Transactions on Plasma Science 42 (2014) 1764–1769. Doi: 10.1109/TPS.2014.2322071.

[34] C. Mistrangelo, L. Bühler, Electric flow coupling in the HCLL blanket concept, Fusion Engineering and Design 83 (2008) 1232–1237. Doi: 10.1016/j.fusengdes.2008.07.004.

[35] S. Molokov, L. Bühler, Liquid metal flow in a U-bend in a strong uniform magnetic field, Journal of Fluid Mechanics 267 (1994) 325–352. Doi: 10.1017/S0022112094001205.

[36] J. Reimann, S. Molokov, I. Platnieks, E. Platacis, MHD-flow in multichannel U-bends: screening experiments and theoretical analysis, in: Fusion Technology 1992, Elsevier, 1993, pp. 1454–1458. Doi: 10.1016/B978-0-444-89995-8.50285-X.

[37] K. Miyazaki, S. Inoue, N. Yamaoka, T. Horiba, K. Yokomizo, Magneto-hydro-dynamic pressure drop of lithium flow in rectangular ducts, Fusion Technology 10 (1986) 830–836. Doi: 10.13182/FST10-830.

[38] A. Tassone, M. Nobili, G. Caruso, Numerical study of the MHD flow around a bounded heating cylinder: Heat transfer and pressure drops, International Communications in Heat and Mass Transfer 91 (2018) 165–175. Doi: 10.1016/j.icheatmasstransfer.2017.12.010.

[39] A. Tassone, L. Gramiccia, G. Caruso, Three-dimensional mhd flow and heat transfer in a channel with internal obstacle, International Journal of Heat and Technology 36 (2018) 1367–1377. Doi: 10.18280/ijht.360428.

[40] C. Alty, Magnetohydrodynamic duct flow in a uniform transverse magnetic field of arbitrary orientation, Journal of Fluid Mechanics 48 (1971) 429–461. Doi: 10.1017/S0022112071001691.

[41] X. Zhang, J. Mao, Y. Chen, C. Pan, Z. Xu, Investigations of liquid metal magnetohydrodynamic rectangular duct flows under inclined transversal magnetic fields, Nuclear Fusion 59 (2019) 056018. Doi: 10.1088/1741-4326/ab0b46.

[42] V. Klüber, L. Bühler, C. Mistrangelo, Numerical investigation of liquid metal flow in square channels under inclined magnetic fields for fusion relevant parameters, Magnetohydrodynamics (0024-998X) 56 (2020) 149–156. Doi: 10.22364/mhd.56.2-3.6.

[43] M. Tillack, A. Ying, H. Hashizume, The effect of magnetic field alignment on heat transfer in liquid metal blanket channels, in: IEEE Thirteenth Symposium on Fusion Engineering, IEEE, 1989, pp. 376–379. Doi: 10.1109/FUSION.1989.102243.

[44] M. J. Bluck, M. J. Wolfendale, An analytical solution to electromagnetically coupled duct flow in MHD, Journal of Fluid Mechanics 771 (2015) 595–623. Doi: 10.1017/jfm.2015.202.

[45] X. Zhang, L. Wang, C. Pan, Effects of inclined transversal magnetic fields on magnetohydrodynamic coupling duct flow states in liquid metal blankets: Under uniform magnetic fields, Nuclear Fusion 61 (2020) 016005. Doi: 10.1088/1741-4326/abbc4c.

[46] O. Zikanov, Y. Listratov, X. Zhang, V. Sviridov, Instabilities in extreme magnetoconvection, in: Computational Modelling of Bifurcations and Instabilities in Fluid Dynamics, Springer, 2019, pp. 401–417. Doi: 10.1007/978-3-319-91494-7_11.

[47] Y. Yan, A. Ying, M. Abdou, Numerical study of magnetoconvection flows in a complex prototypical liquid-metal fusion blanket geometry, Fusion Engineering and Design 159 (2020) 111688. Doi: 10.1016/j.fusengdes.2020.111688.

[48] F. Roca Urgorri, I. Fernàndez, Internal Deliverable BB-3.2.1-T007-D002, EFDA D 2PF8DT ver. 1.1, Design Engineering for WCLL - 2020 activities), Eurofusion, 2020. Available online for EUROfusion members at https://idm.eurofusion.org/?uid=2PF8DT.

[49] C. Alberghi, L. Candido, R. Testoni, M. Utili, M. Zucchetti, Magneto-convective effect on tritium transport at breeder unit level for the wcll breeding blanket of demo, Fusion Engineering and Design 160 (2020) 111996. Doi: 10.1016/j.fusengdes.2020.111996.

[50] Z. Tao, M.-J. Ni, Analytical solutions for MHD flow at a rectangular duct with unsymmetrical walls of arbitrary conductivity, Science China Physics, Mechanics & Astronomy 58 (2015) 1–18. Doi: 10.1007/s11433-014-5518-x.